Supplementary Material:

Observation of Degenerate Merging Bound States in the Continuum in All-Dielectric Metasurfaces

Chaobiao Zhou[1,#,*], Haoxuan He[1,#,*], Zhenchu Fu[2,3,4,#], Shaojun You[5], Lulu Wang[1], Jing Huang[1], Xia Yan[1], Xiaoshuang Chen[2,3,4], Wei Lu[2,3,4], Lujun Huang[5,*], Guanhai Li[2,3,4,*]

[1]*School of Physics and Mechatronic Engineering, Guizhou Minzu University, Guiyang 550025, China.*

[2]*State Key Laboratory of Infrared Physics, Shanghai Institute of Technical Physics, Chinese Academy of Sciences, 500 Yu Tian Road, Shanghai 200083, China.*

[3]*Hangzhou Institute for Advanced Study, University of Chinese Academy of Sciences, No.1 SubLane Xiangshan, Hangzhou 310024, China.*

[4]*Shanghai Research Center for Quantum Sciences, 99 Xiupu Road, Shanghai 201315, China*

[5]*State Key Laboratory of Precision Spectroscopy, School of Physics and Electronic Sciences, East China Normal University, Shanghai 200241, China*

[#]*These authors contributed equally: Chaobiao Zhou, Haoxuan He, Zhenchu Fu,*

**E-mail: ghli0120@mail.sitp.ac.cn; cbzhou@gzmu.edu.cn; ljhuang@phy.ecnu.edu.cn; hxhe@gzmu.edu.cn*

Supplementary Note 1：Group theory of degenerate

Supplementary Note 2：Degeneracy characteristics of modes in several C_{4v} scenarios

Supplementary Note 3: Scale rule of the Q-factors with respect to *k*

Supplementary Note 4: Far-field polarization states

Supplementary Note 5: The distribution of electric and magnetic fields for degenerate and non-degenerate states.

Supplementary Note 6: Multipole decomposition of degenerate and non-degenerate quasi-BICs

Supplementary Note 7: Schematic of the experimental setup for optical characterization

Supplementary Note 8: Summary of measured Q-factors in the quasi-BICs

Supplementary Note 9: Normalized experimental reflection spectra and Fano fitting under different *L*

Supplementary Note 1： Group theory of degenerate

According to group theory, the eigenstates of metasurface structures can be characterized by irreducible representations of point groups. For a metasurface exhibiting C_{4v} symmetry, there are six irreducible representations: A_1, A_2, B_1, B_2, $E^{(1)}$, and $E^{(2)}$, as detailed in **Table 1**. By integrating these irreducible representations with those of the eigenfield, we gain a deeper understanding of the radiative and degenerate characteristics of the eigenmodes[1-4].

$E^{(1)}$ and $E^{(2)}$ correspond to double degeneracy modes, indicating that within the C4v structure of a square lattice, these modes rotate by 90° before overlapping. If this characteristic is disrupted, they transition into non-degenerate modes. In the configuration illustrated in Figure 2(a), adjusting device parameters can yield two merging BICs at the Γ point. Owing to the symmetry inherent in C_{4v}, these states can exhibit degenerate properties.

Table 1. Character table of the C_{4v} point group.

C_{4v}	E	$2C_4$	C_2	$2\sigma_v$	$2\sigma_d$
A_1	1	1	1	1	1
A_2	1	1	1	-1	-1
B_1	1	-1	1	1	-1
B_2	1	-1	1	-1	1
E	2	0	-2	0	0

Supplementary Note 2：Degeneracy characteristics of modes in several C_{4v} scenarios

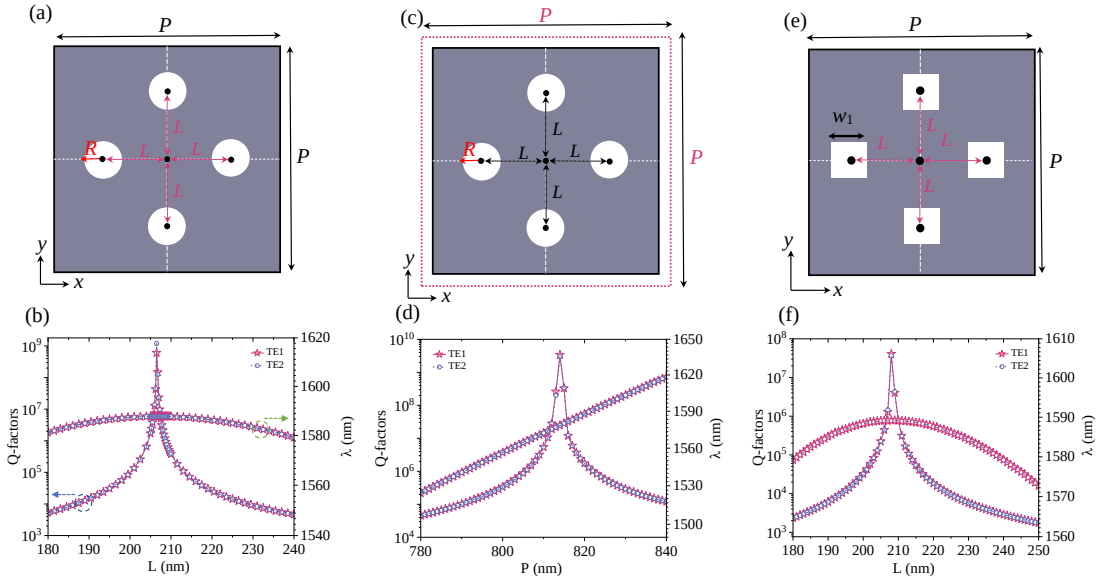

Figure S1. (a) Four circular holes are symmetrically arranged along the axis within the unit cell, featuring the period P=820 nm and a variable parameter L. (c) Maintaining L constant while varying the period P. (e) Modifying the original circular hole into a square hole, keeping P unchanged while altering L. (b), (d), and (f) The Q-factors and corresponding wavelengths exhibit variations with respect to L and P. As the structural parameters transition from the critical position of merging BICs, the topological charge gradually deviates from the Γ point. The Q-factors at the Γ point exhibit an attenuation trend; however, due to symmetry constraints inherent in the structure, they consistently remain in a degenerate state.

Supplementary Note 3: Scale rule of the Q-factors with respect to *k*

Generally, when the topological charge carried by a BIC is ±1, the Q varies with the wavevector (k) according to the following relationship: $Q \propto 1/k^2$. In our proposed structure, the accidental BIC located at the off-Γ point carries a topological charge of +1. When L=205 nm, the corresponding TE modes exhibit the following dependencies: for TE1 mode, $Q \propto k^{-2.4}$; and for TE2 mode, $Q \propto k^{-2.1}$. Similarly, when L= 206 nm, the TE1 mode follows $Q \propto k^{-2.4}$, while the TE2 mode adheres to $Q \propto k^{-2.1}$, as illustrated in **Figures S2(a) and (b)**. These results indicate that the Q-factor generally follows the expected attenuation law with respect to k.

The merging BICs involves the integration of multiple topological charges, and its Q-factor attenuation behavior cannot be adequately described by the attenuation formula applicable to a single topological charge. This phenomenon manifests as a superposition of contributions from each individual topological charge. Unlike traditional merging BICs, our study focuses on merging BICs that lack symmetry-protected BICs; instead, they are entirely formed through the accidental BICs. At the state of merging, L is measured at 206.55 nm. The attenuation laws for two modes, TE1 and TE2, are represented as $Q \propto k^{-4.1}$ and $Q \propto k^{-4.2}$, respectively, as illustrated in **Figure S2(c)**. It is evident that these merging BICs significantly enhance the robustness of Q within k space. Upon completion of the merging process, the topological charge gradually shifts away from the Γ point. These distinctive attenuation characteristics reflect dynamic changes occurring during both the merger and separation processes involving topological charges associated with merging BICs.

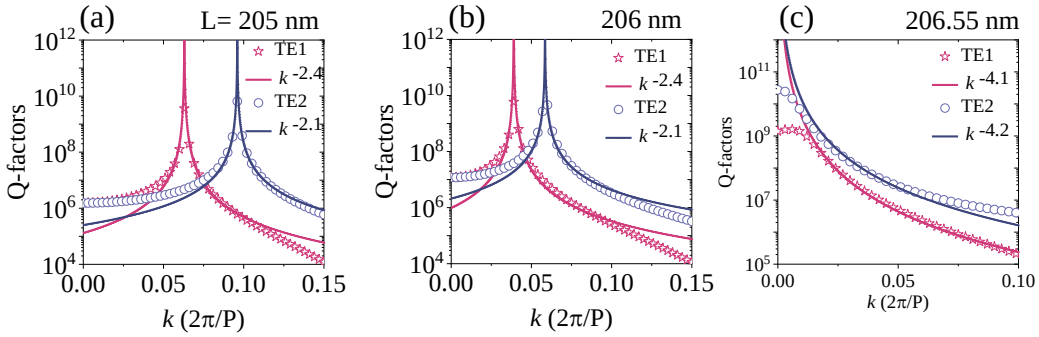

Figure S2. Attenuation relationship between Q and k. (a)-(d) show the attenuation relationships between Q and k for the TE1 and TE2 modes for L=205 nm, 206 nm, and 206.55 nm, respectively.

Supplementary Note 4: Far-field polarization states

The projected polarization vector $\boldsymbol{k}_{\square}\left(k_x, k_y\right)$ is defined in the *x*-*y* plane and can be obtained through the following integral[5-7]:

$$c(k) = (c_x, c_y, c_z) = \frac{1}{\iint_{Cell} dxdy} \iint_{Cell} e^{ik_x x + ik_y y} E(x, y, z) dxdy$$

The integral surface lies on the *x*-*y* plane, either above or below the structure, corresponding to upward or downward radiation. In this context, the polarization vector in the *x*-*y* plane is directly represented as follows:

$$c(k_{\square}) = c_x(k_{\square})\vec{x} + c_y(k_{\square})\vec{y}$$

For the in-plane two-dimensional electric field components $c_x(k_{\square}) = E_x$, and $c_y(k_{\square}) = E_y$, the Stokes parameters are given by:

$$\begin{aligned} S_0 &= |E_x|^2 + |E_y|^2 \\ S_1 &= |E_x|^2 - |E_y|^2 \\ S_2 &= 2\,\mathrm{Re}(E_x^* E_y) = 2|E_x E_y|\cos\phi \\ S_3 &= 2\,\mathrm{Im}(E_x^* E_y) = 2|E_x E_y|\sin\phi \end{aligned}$$

Here, $\phi = \arg(E_x) - \arg(E_y)$ represents the phase difference between the *x*-polarization and *y*-polarization components. The incident Stokes parameters are normalized to 1, ensuring that all parameters satisfy specified conditions $S_0 = S_1 + S_2 + S_3$. The ellipticity of far-field radiation is defined as $\rho = S_3 / S_0$.

Supplementary Note 5: The distribution of electric and magnetic fields for degenerate and non-degenerate states.

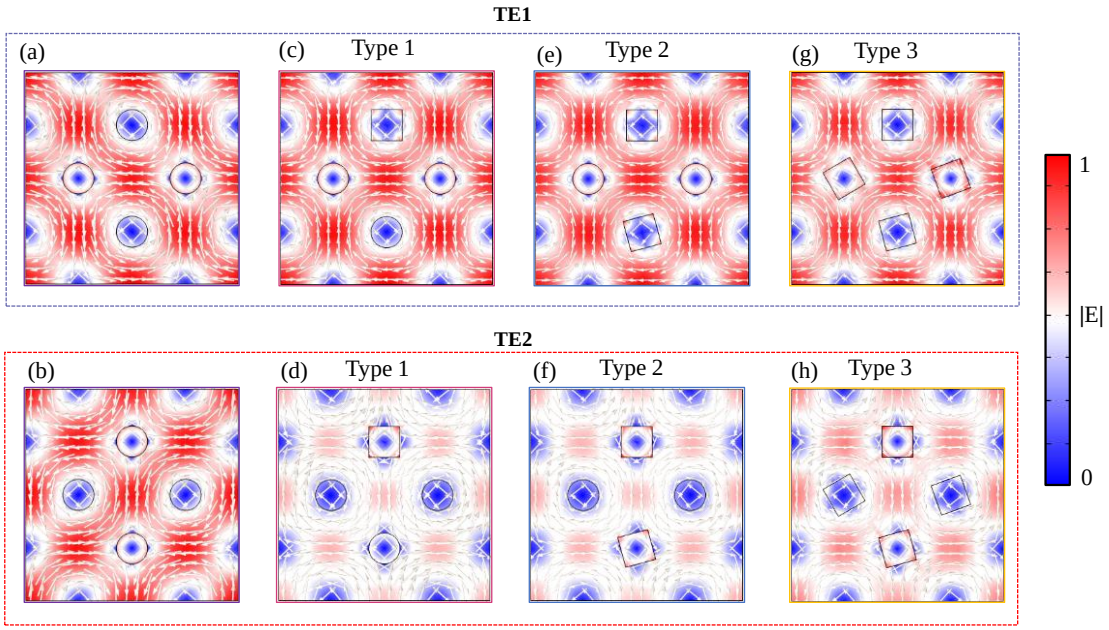

Figure S3. (a), (b) The electric field intensity and vector distribution of TE1 and TE2 in the degenerate state. The electric fields of TE1 and TE2 completely overlap after rotating 90°, confirming the double degenerate characteristics. (c)-(h) The electric field distributions of TE1 and TE2 in the three non-degenerate states cannot completely overlap when rotated 90°, confirming the characteristics of non-degenerate.

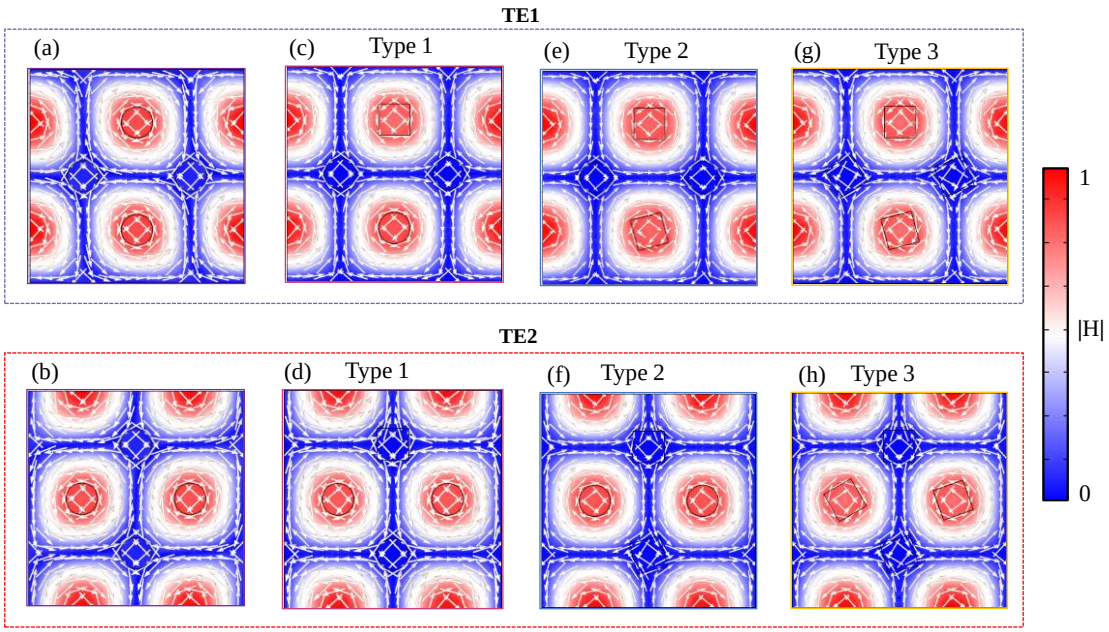

Figure S4. Magnetic field distribution of TE1 and TE2 for degenerate states in (a)-(b), for non-degenerate states in (c)-(h).

Supplementary Note 6: Multipole decomposition of degenerate and non-degenerate quasi-BICs

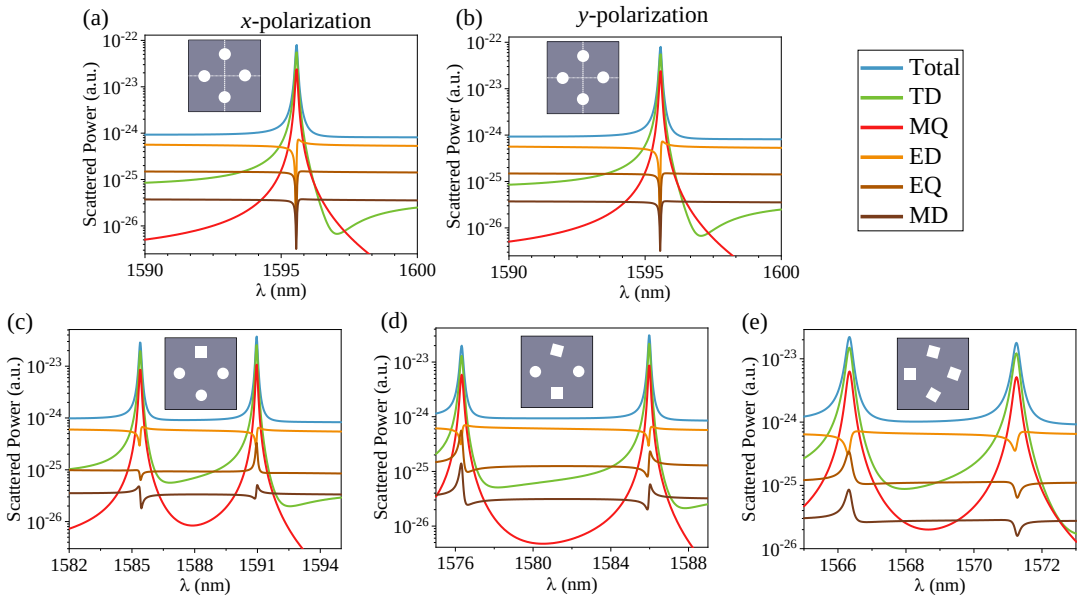

Figure S5. (a), (b) The multipole scattering power of the unit cell under *x* and *y* polarized light irradiation at *L*=220 nm, *R*=60 nm, and *P*=820 nm. It can be seen that their multipole contributions are consistent, and the toroidal dipole (TD) dominate the resonance in both cases, further confirming their degenerate characteristics. (c)-(e) Multipole decomposition of Type 1, Type 2 and Type 3 at *L*=220 nm, *R*=60 nm, *P*=820 nm and *w*=104 nm. Due to the breaking of structural symmetry, the previous degenerate mode splits into two resonant modes, and their multipole contributions are consistent with those of the previous degenerate mode, revealing the intrinsic connection between the degenerate and non-degenerate modes.

Supplementary Note 7: Schematic of the experimental setup for optical characterization.

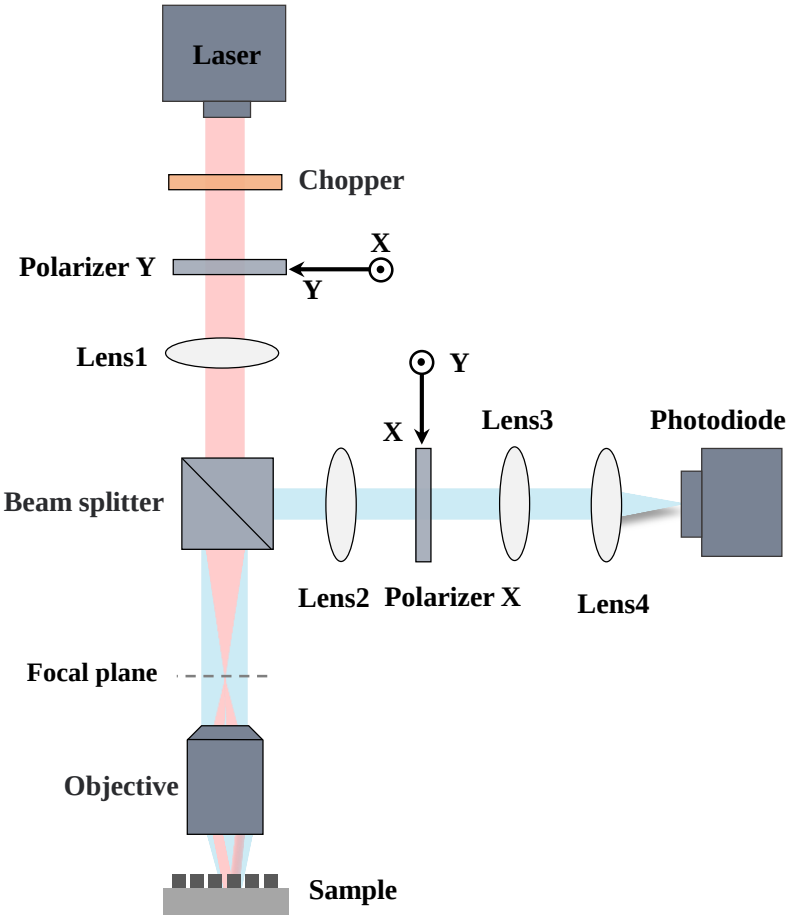

Figure S6. Schematic of the experimental setup for optical characterization. The red and blue lines represent the incident light and direct reflection from the sample, respectively.

Supplementary Note 8: Normalized experimental reflection spectra and Fano fitting under different *L*

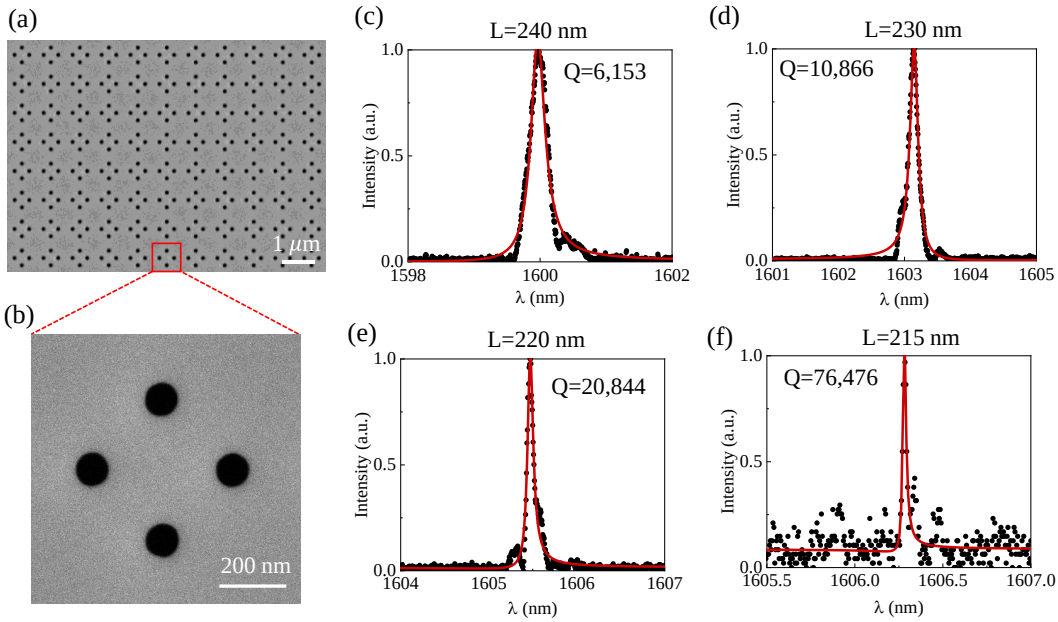

Figure S7. (a), (b) SEM images of symmetry structure and the corresponding locally enlarged images, (c)-(f) Normalized reflection spectra and Fano fitting [19] results for different L values. The black dots represent the experimental data, while the solid red line indicates the fitted spectral line. The Q is calculated by dividing the resonance wavelength by the line width.

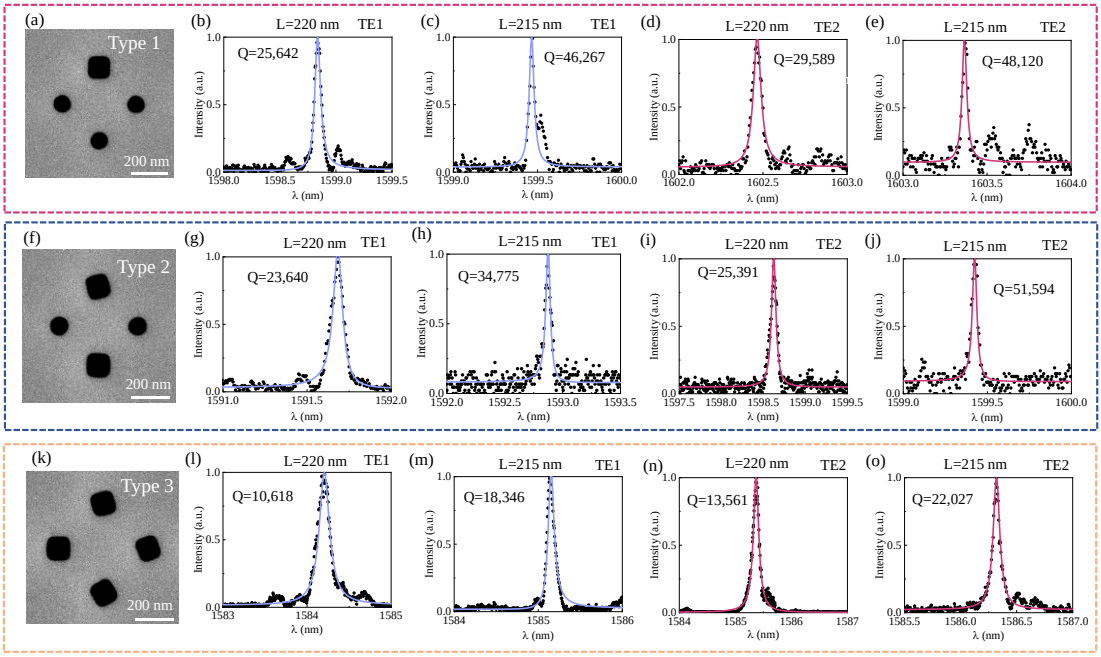

Figure S8. SEM images of unit cell for three asymmetry structures (Type 1, Type 2 and Type 3), and the normalized experiment reflection spectra and Fano fitting results at different L values.

Supplementary Note 9: Summary of measured Q-factors in the quasi-BICs

Tabla 2. Summary of measured Q-factors in the quasi-BICs.

Mechanism	Q	λ (nm)	Structure	Substrate	References
SP-BIC	4,700	1551.4	InGaAsP nanopillar	Y	2017, Nature[8]
SP-BIC	2750	825	GaAs nanopillar	Y	2018, Nat. Nanotechnol.[9]
SP-BIC	18,511	1588	Si double-notched nanodisks	Y	2019, Phys. Rev. Lett.[10]
SP-BIC	1,000	1511.8	GaAs notch nanodisks	Y	2022, Science[11]
SP-BIC	36,694	1516	Si double holes	Y	2023, Adv. Funct. Mater.[12]
SP-BIC	2,663	618	TiO_2 slant square nanohole	Y	2023, Nature[13]
SP-BIC	3,425	1527	Polymer nanocubes	Y	2024, Laser Photonics Rev.[14]
SP-BIC	22,633	1520	Si nanohole dimer	Y	2024, Appl. Phys. Rev.[15]
SP-BIC	101,486	1560	Si shallow pair-rod	Y	2025, Nano. Lett.[16]
Merging BIC	490,000	1568.3	Si PCS	N	2019, Nature[17]
Merging BIC	7,250	1595	InGaAsP PCS	N	2021, Nat. Commun.[18]
Merging BIC	**326,413**	**1599**	**Si nanohole tetramer**	**Y**	**This work**

References

[1] C.F. Doiron, I. Brener and A. Cerjan, Realizing symmetry-guaranteed pairs of bound states in the continuum in metasurfaces. *Nat. Commun.*, **2022**. *13*, 7534.

[2] C.F. Doiron, I. Brener and A. Cerjan, Dual-Band Polarization Control with Pairwise Positioning of Polarization Singularities in Metasurfaces. *Phys. Rev. Lett.*, **2024**. *133*, 213802.

[3] M.D. Onur Kilic, Gordon Kino, and Olav Solgaard, Controlling uncoupled resonances in photonic crystals through breaking the mirror symmetry. *Opt. Express*, **2008**. *16*, 13090-13103.

[4] A.C. Overvig, S.C. Malek, M.J. Carter, S. Shrestha, and N. Yu, Selection rules for quasibound states in the continuum. *Phys. Rev. B*, **2020**. *102*, 035434.

[5] T. Yoda and M. Notomi, Generation and Annihilation of Topologically Protected Bound States in the Continuum and Circularly Polarized States by Symmetry Breaking. *Phys. Rev. Lett.*, **2020**. *125*, 053902.

[6] W. Ye, Y. Gao and J. Liu, Singular Points of Polarizations in the Momentum Space of Photonic Crystal Slabs. *Phys. Rev. Lett.*, **2020**. *124*, 153904.

[7] W. Liu, B. Wang, Y. Zhang, J. Wang, M. Zhao, F. Guan, X. Liu, L. Shi, and J. Zi, Circularly Polarized States Spawning from Bound States in the Continuum. *Phys. Rev. Lett.*, **2019**. *123*, 116104.

[8] A. Kodigala, T. Lepetit, Q. Gu, B. Bahari, Y. Fainman, and B. Kante, Lasing action from photonic bound states in continuum. *Nature*, **2017**. *541*, 196-199.

[9] S.T. Ha, Y.H. Fu, N.K. Emani, Z. Pan, R.M. Bakker, R. Paniagua-Domínguez, and A.I. Kuznetsov, Directional lasing in resonant semiconductor nanoantenna arrays. *Nat. Nanotechnol.*, **2018**. *13*, 1042-1047.

[10] Z. Liu, Y. Xu, Y. Lin, J. Xiang, T. Feng, Q. Cao, J. Li, S. Lan, and J. Liu, High-Q Quasibound States in the Continuum for Nonlinear Metasurfaces. *Phys. Rev. Lett.*, **2019**. *123*, 253901.

[11] T. Santiago-Cruz, S.D. Gennaro, O. Mitrofanov, S. Addamane, J. Reno, I. Brener, and M.V. Chekhova, Resonant metasurfaces for generating complex quantum states. *Science*, **2022**. *377*, 991-995.

[12] S.L. Lujun Huang, Chaobiao Zhou, Haozong Zhong, Shaojun You, Lin Li, Ya Cheng, and Andrey E Miroshnichenko, Realizing Ultrahigh-Q Resonances Through Harnessing Symmetry-Protected Bound States in the Continuum. *Adv. Funct. Mate.*, **2023**. *34*, 2309982.

[13] Y. Chen, H. Deng, X. Sha, W. Chen, R. Wang, Y.H. Chen, D. Wu, J. Chu, Y.S. Kivshar, S. Xiao, and C.W. Qiu, Observation of intrinsic chiral bound states in the continuum. *Nature*, **2023**. *613*, 474-478.

[14] C. Fang, R. Kanyang, Y. Ji, Y. Zhang, J. Yang, D. Wang, Y. Liu, X. Gan, G. Han, and Y. Hao, Multiple High‐Q Optical Modes in a Polymer‐Lithium Niobate Integrated Metasurface. *Laser Photonics Rev.*, **2023**. *18*, 2300900.

[15] H. Zhong, L. Huang, S. Li, C. Zhou, S. You, L. Li, Y. Cheng, and A.E. Miroshnichenko, Toroidal dipole bound states in the continuum in asymmetric dimer metasurfaces. *Appl. Phys. Rev.*, **2024**. *11*, 031404.

[16] K. Watanabe, T. Nagao and M. Iwanaga, Low-Contrast BIC Metasurfaces with Quality Factors Exceeding 100,000. *Nano Lett.*, **2025**. *25*, 2777-2784.

[17] J. Jin, X. Yin, L. Ni, M. Soljacic, B. Zhen, and C. Peng, Topologically enabled ultrahigh-Q guided resonances robust to out-of-plane scattering. *Nature*, **2019**. *574*, 501-504.

[18] M.S. Hwang, H.C. Lee, K.H. Kim, K.Y. Jeong, S.H. Kwon, K. Koshelev, Y. Kivshar, and H.G. Park, Ultralow-threshold laser using super-bound states in the continuum. *Nat. Commun.*, **2021**. *12*, 4135.

[19] W.X. Lim, M. Manjappa, P. Pitchappa and R. Singh, Shaping high‐Q planar fano resonant metamaterials toward futuristic technologies. *Adv. Opt. Mater.*, **2018**. *6*, 1800502.